International Journal of Nanomedicine

Dovepress
open access to scientific and medical research

Open Access Full Text Article

ORIGINAL RESEARCH

Glucose-Regulated Protein 78 Targeting ICG and DOX Loaded Hollow Fe_3O_4 Nanoparticles for Hepatocellular Carcinoma Diagnosis and Therapy

Yushen Jin[1], Zhongquan Cheng[2], Zhu Yuan[2], Yang Du[3], Jie Tian[3], Bing Shao[1,4]

[1]Beijing Key Laboratory of Diagnostic and Traceability Technologies for Food Poisoning, Beijing Centre for Disease Prevention and Control, Beijing, 100013, People's Republic of China; [2]Department of General Surgery, Capital Medical University, Beijing Friendship Hospital, Beijing, 100050, People's Republic of China; [3]CAS Key Laboratory of Molecular Imaging, Key Laboratory of Molecular Imaging, Institute of Automation, Chinese Academy of Sciences, Beijing, 100190, People's Republic of China; [4]College of Veterinary Medicine, China Agricultural University, Beijing, 100193, People's Republic of China

Correspondence: Bing Shao; Jie Tian, Email shaobingch@sina.com; jietian@ia.ac.cn

Purpose: Liver cancer is considered as the third leading cause of cancer-related deaths, with hepatocellular carcinoma (HCC) accounting for approximately 90% of liver cancers. Improving the treatment of HCC is a serious challenge today. The primary objective of this study was to construct SP94-Fe_3O_4@ICG&DOX nanoparticles and investigate their potential diagnosis and treatment effect benefits on HCC.

Methods: Firstly, we synthesized and characterized SP94-Fe_3O_4@ICG&DOX nanoparticles and confirmed their in vitro release behavior, photothermal and photodynamic performance. Moreover, the in vivo imaging capability was also observed. Finally, the inhibitory effects on Hepa1-6 in vitro and in vivo were observed as well as biosafety.

Results: SP94-Fe_3O_4@ICG&DOX nanoparticles have a size of ~22.1 nm, with an encapsulation efficiency of 45.2% for ICG and 42.7% for DOX, showing excellent in vivo MPI and fluorescence imaging capabilities for precise tumor localization, and synergistic photo-chemotherapy (pH- and thermal-sensitive drug release) against tumors under irradiation. With the assistance of a fluorescence molecular imaging system or MPI scanner, the location and contours of the tumor were clearly visible. Under a constant laser irradiation (808 nm, 0.6 W/cm^2) and a set concentration (50 μg/mL), the temperature of the solution could rapidly increase to ~45 °C, which could effectively kill the tumor cells. It could be effectively uptaken by HCC cells and significantly inhibit their proliferation under the laser irradiation (100% inhibition rate for HCC tumors). And most importantly, our nanoparticles exhibited favorable biocompatibility with normal tissues and cells.

Conclusion: This versatile agent can serve as an intelligent and promising nanoplatform that integrates multiple accurate diagnoses, precise positioning of cancer tissue, and effective coordination with synergistic tumor photodynamic therapy.

Keywords: porous hollow structure, magnetic particle imaging, fluorescence imaging, synergistic treatment, theranostics

Introduction

Hepatocellular carcinoma (HCC), accounts for approximately 90% of liver cancers, is a primary malignancy tumor.[1,2] Liver cancer is considered the third leading cause of cancer-related deaths[3] with nearly 830, 000 deaths globally in 2020, of which 390,000 occurred in China.[4] Due to insufficient screening, HCC is usually diagnosed at an advanced stage.[5,6] Clinically, local recurrence of residual tiny tumors after radical resection is one of the main causes leading to treatment failure. Photothermal therapy (PTT) and photodynamic therapy (PDT) have been recognized as common phototherapy regimens for tumor treatment; however, their therapeutic outcomes have been limited owing to the limited penetration depth of light and low therapeutic accuracy.[7–9] To further prolong the survival time of patients and minimize tumor recurrence, it is imperative to develop multimodal tumor treatment strategies by combining PTT and PDT with other therapeutic methods and multimodal imaging-guided therapies.

Received: 25 July 2023
Accepted: 16 December 2023
Published: 8 January 2024

Graphical Abstract

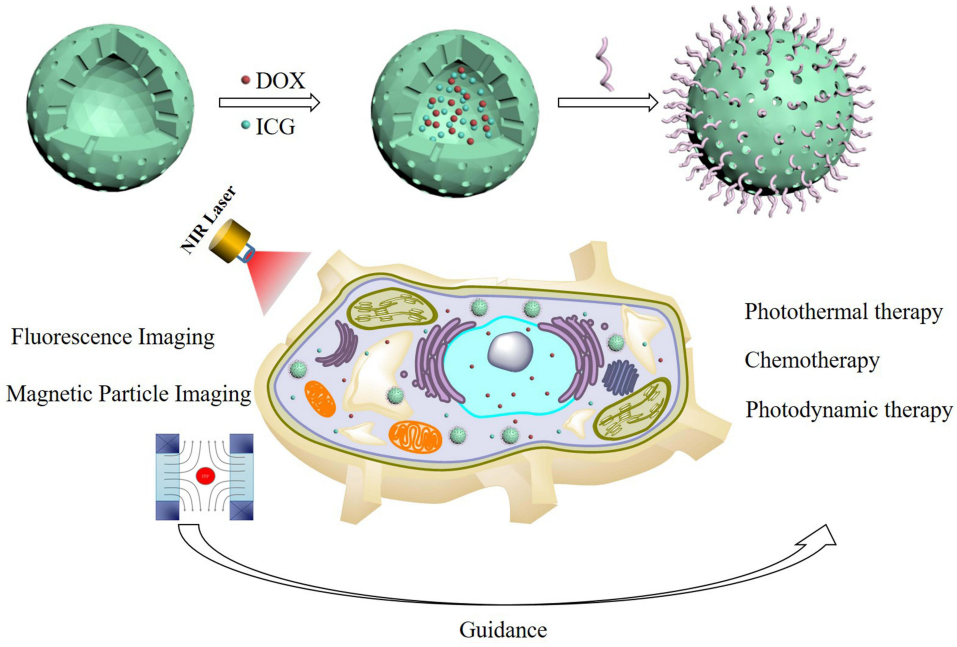

Magnetic particle imaging (MPI) has attracted increasing attention owing to its high mass sensitivity, high spatio-temporal resolution, zero tissue depth signal attenuation, and lack of ionizing radiation.[10–14] Magnetic nanoparticles, especially iron oxide nanoparticles, are preferred materials for MPI contrast agents.[14,15] Iron oxide nanoparticles are widely used in MP imaging.[16,17] To optimize the MPI signal, it is necessary to adjust the size and size distribution of the nanoparticles according to the excitation frequency of MPI, which determines the relaxation mechanism and distribution of relaxation times.[18] Research has shown that iron oxide magnetic nanoparticles with a core diameter of 26–27 nm provide excellent performance for MPI, and modeling studies predict 25–30 nm is the optimum diameter for iron oxide magnetic nanoparticles.[19,20] Otherwise, size uniformity is important for MP imaging.[18] Solid Fe_3O_4 nanoparticles are dependent on the modified coatings on the surface of Fe_3O_4 to provide chemical coordination/coupling sites for drugs, targeting ligands, and other therapeutic reagents,[21,22] however, the cavity of the hollow Fe_3O_4 nanoparticles can be used to encapsulate drugs, and their modified coatings can be used to conjugate targeted ligands.[23] Thus, hollow Fe_3O_4 is more suitable for targeted drug delivery. To date, there have been few reports on hollow Fe_3O_4 nanoparticles for MP imaging, which may be because of the difficulty in synthesizing hollow Fe_3O_4 with small and uniform sizes. Compared with other imaging modalities, fluorescence imaging is suitable for detecting cancerous lesions during the therapeutic process because of its high sensitivity and convenient operation.[24–30] Thus, the combination of fluorescence imaging and MPI may be a promising multimodal technique to accurately identify HCC lesions with high sensitivity and spatial resolution.

Glucose-regulated protein 78 (GRP78) is a stress-induced endoplasmic reticulum chaperone protein that is highly expressed in cancer cells[31,32] into solid tumor cells, the GRP78 can be secreted to promote tumor angiogenesis, differentiation, and tumor cell proliferation.[33–35] The increased expression of GRP78 is involved in the invasion and metastasis of many human cancers such as gastric cancer, prostate cancer, and HCC.[36–40] SP94, a receptor of GRP78, can effectively bind to GRP78 on the membranes of HCC cells.[38] In our previous work, we developed an SP94-targeted dual-modal imaging contrast agent that could effectively guide the detection and resection of HCC to avoid false-negative detection.[24] Yan et al fabricated SP94-Fn-Dox (HccFn-Dox), which could effectively deliver anti-HCC drugs without damaging healthy tissues.[38] Therefore, SP94 has a clinical potential for guiding HCC therapy.

In this study, we constructed a hollow Fe_3O_4 nanoparticle-based nanomedicine system modified with SP94 (SP94-Fe_3O_4@ICG&DOX) to achieve controlled drug release, accurate detection, and synergetic therapy for HCC. DOX and ICG were stored in porous hollow nanoparticles, and their release was modulated in response to near infrared (NIR) laser irradiation and the pH of the surrounding environment. The in vitro and in vivo results showed that our nanomedicine system achieved an effective diagnosis of HCC using MPI and delineated tumor boundaries using fluorescence imaging to guide therapy. Additionally, SP94-Fe_3O_4@ICG&DOX nanoparticles provided a robust tumor inhibition effect through the combination of controlled chemotherapy and phototherapy. Therefore, this pH- and photothermal-responsive drug delivery system, which had good biocompatibility and targeting ability, with favorable biocompatibility and targeting capability could be an intelligent agent for diagnosis and synergetic chemo-photo therapy of HCC therapy.

Materials and Methods

Materials

Iron pentacarbonyl ($Fe(CO)_5$), 1-octadecene (90%), oleylamine (70%), oleic acid (OA, 90%), trimethylamine N-oxide ($(CH_3)_3NO$, 98%), N-hydroxysuccinimide (NHS, 98%), and N-(3-Dimethylaminopropyl)-N'-N-ethylcarbodiimide hydrochloride (EDC·HCl, 98%) were from Sigma-Aldrich. The SP94 peptide (with slight modifications, sequence: NH_2-GCESFSIIHTPILPL-COOH) was purchased from China Peptides Co., Ltd. ICG was acquired from Ruixi Bio Technology (Beijing, China). DOX was obtained from Beijing HVSF United Chemical Materials Co., Ltd. 2',7'-dichlorofluorescin diacetate (H_2DCFDA) and dihydroethidium (DHE) were purchased from Shanghai Maokang Biotechnology Co., Ltd. CCK8 and LDH assay kit were purchased from Beyotime Biotechnology. The Hepa1-6 cells were purchased from Cell Bank of the Chinese Academy of Sciences (Shanghai, China).

Preparation of Hollow Fe_3O_4 Nanoparticles

The Fe_3O_4 hollow nanoparticles were prepared via high-temperature thermal decomposition method with two steps: 1) 20 mL 1-octadecene and 0.3 mL oleylamine were mixed in a four-necked flask and the moisture and oxygen could be eliminated by stirring with a mechanical blender and bubbling nitrogen through the mixture solution at 120 °C for 30 min. When the temperature of the mixture slowly reached 180 °C, 0.7 mL of $Fe(CO)_5$ was quickly injected into the mixture and the solution was held at 180 °C for 30 min. The mixture was then cooled to room temperature and the supernatant was discarded. Fe/Fe_3O_4 nanoparticle seeds were precipitated by adding 30 mL of isopropanol. Purified nanoparticles were re-dispersed in hexane in the presence of oleylamine. 2) 80 mg of Fe/Fe_3O_4 nanoparticles seeds in hexane were quickly injected into a mixture of 1-octadecene (20 mL) and $(CH_3)_3NO$ (30 mg) and degassed under nitrogen at 130 °C for 1 h. The mixture was maintained at 130 °C for 26 h, and then continuously heated to 250 °C for 1 h. After cooling to room temperature, the mixture was precipitated by adding 40 mL acetone and magnetic separation. The purified product was obtained by repeating this procedure twice. Finally, the resulting hollow Fe_3O_4 nanoparticles were dispersed in hexane.

Synthesis of SP94-Fe_3O_4@ICG&DOX Nanoparticles

The hydrophobic hollow Fe_3O_4 nanoparticles were transferred to the water phase via a ligand exchange reaction. 6 mL tetrahydrofuran (THF) containing 50 mg of 3.4-dihydroxyhydrocinnamic acid (DHCA) was heated to 50 °C under nitrogen flow. Then, 20 mg of the hydrophobic hollow Fe_3O_4 nanoparticles dispersed in 1 mL of THF was added dropwise over 6 h. The resultant mixture was cooled to room temperature, and the hollow Fe_3O_4 nanoparticles were collected by magnetic separation and re-dispersed in water.

Fe_3O_4@ICG&DOX nanoparticles were fabricated using an extremely simple mixing method at room temperature. Briefly, 10 mg carboxyl-functionalized hollow Fe_3O_4 nanoparticles, 5 mg ICG, and 10 mg DOX were dissolved in 20 mL pure water. The mixture was sonicated with a probe-type sonicator for 5 min at 150 W (3 s pulse and 7 s rest) and stirred in the dark at room temperature for 24 h. The free DOX and ICG were removed by centrifugation (14, 000 rpm, 30 min), followed by washing with DI water three times. Finally, the SP94 peptide was conjugated to the surface of Fe_3O_4

@ICG&DOX using EDC/HCl/NHS. The unbound SP94 peptide was removed by centrifugation and washed three times with DI water. The purified nanoparticles were lyophilized and stored in the dark until further use.

The loading efficiency of ICG and DOX was calculated using the following equation:

$$\text{Loading efficiency } (\%) = \frac{W_{\text{initial drug}} - W_{\text{drug in supernatant}}}{W_{\text{initial drug}}} \times 100$$

Characterization of SP94-Fe_3O_4@ICG&DOX Nanoparticles

The hydrodynamic size and particle dispersion index (PDI) of the SP94-Fe_3O_4@ICG&DOX nanoparticles were measured using a Malvern Zetasizer. The morphology of SP94-Fe_3O_4@ICG&DOX nanoparticles was analyzed using a Hitachi HT7800 transmission electron microscope (TEM, Hitachi, Japan). UV-Vis–NIR absorption spectra were acquired using a UV/Vis spectrophotometer. Fluorescence spectra were obtained using a fluorescence spectrometer. The porosity of the hollow Fe_3O_4 nanoparticles was determined using the Barrett–Joyner–Halenda method and an ASAP2460 system.

In vitro Drug Release Assays

To examine the in vitro release behavior of SP94-Fe_3O_4@ICG&DOX nanoparticles, 1 mg of nanoparticles was dispersed in 1 mL of phosphate-buffered saline (PBS, pH7.4 or pH 5.5). The supernatants of the solutions were collected using a magnet under gentle oscillations at different time intervals. To further evaluate NIR-induced drug release, the SP94-Fe_3O_4@ICG&DOX nanoparticle dispersion was irradiated with an NIR laser (808 nm, 0.6 W/cm^2) for 5 min at a predetermined time point, followed by a certain interval without irradiation. At a predetermined time, supernatants were collected by magnetic attraction at different times under gentle oscillation. The amounts of DOX and ICG released were determined by UV-Vis-NIR absorption spectroscopy.

Photothermal Performance of SP94-Fe_3O_4@ICG&DOX Nanoparticles

To investigate the photothermal effect of SP94-Fe_3O_4@ICG&DOX nanoparticles, nanoparticles solutions with different concentrations and ultrapure water were irradiated with an 808-nm laser (0.6 W/cm^2) for 10 min. The temperature increase of each solution was recorded using an inserted thermocouple probe. To ensure a homogeneous heat distribution during laser irradiation, the solutions were magnetically stirred continuously.

To further investigate the photothermal stability of the SP94-Fe_3O_4@ICG&DOX nanoparticles, five cycles of NIR laser irradiation were performed. In brief, nanoparticles at a concentration of 50 μg/mL were irradiated with 808 nm laser (0.6 W/cm^2) for 10 min, followed by turning off the laser source for 11 minutes, and repeating this cycle for five times.

Single Oxygen Detection

Single oxygen generation by SP94-Fe_3O_4@ICG&DOX nanoparticles was detected by fluorescence spectrophotometry, using H_2DCFDA as an indicator. Briefly, a certain amount of SP94-Fe_3O_4@ICG&DOX were mixed with H_2DCFDA (1 μM) in water containing 2% DMSO and exposed to an 808 nm laser (0.6 W/cm^2). The increase in the fluorescence intensity at 529 nm (Ex 504 nm) was used to evaluate the production of single oxygen.

Cellular Uptake

The uptake of SP94-Fe_3O_4@ICG&DOX nanoparticles into Hepa1-6 cells was assessed using a Leica DMI6000 inverted microscope and an Accuri C6 flow cytometer for qualitative and quantitative analyses, respectively.

For qualitative analysis, 1×10^5 Hepa1-6 cells were seeded on a 6-well plate. When the cell density was > 90%, 0.05 mg/mL FITC labelled Fe_3O_4@ICG&DOX, or SP94-Fe_3O_4@ICG&DOX were added and further incubated for another 4 h at 37 °C. The cells were washed with PBS for three times, and fixed with 4% paraformaldehyde for 20 min. After washing with PBS, the nuclei of the cells were stained with the nuclear dye 4',6-diamidino-2-phenylindole (DAPI). The cells were observed under a Leica DMI6000 inverted microscope. The binding of SP94-Fe_3O_4@ICG&DOX nanoparticles to cells was further analyzed using Perls' Prussian blue staining. Subsequent experiments were with

a similar procedure to the above experiments, except for replacing DAPI with a mixed solution (10% potassium ferrocyanide: 20% HCl, 1:1). The cells were observed under a Leica DMI6000 inverted microscope.

For quantitative analysis, the cells were seeded in a 6-well plate at a density of 1×10^5 cells per well. When the cell confluence reached over 90%, different concentrations of FITC labelled Fe_3O_4@ICG&DOX or SP94-Fe_3O_4 @ICG&DOX were added and incubated for 4 h. The fluorescence intensity of the cells was analyzed using an Accuri C6 flow cytometer.

For ROS (including single oxygen and superoxide anion) detection, ROS formation was monitored using a high-content analysis system (Operetta CLS, PerkinElmer, USA) using DCFH-DA and DHE as indicators. 1×10^5 Hepa1-6 cells were seeded in 96-well glass-bottom plates. After incubation for 24 h, Fe_3O_4@ICG&DOX or SP94-Fe_3O_4 @ICG&DOX was added and incubated for another 4 h at 37 °C. After washing the cells three times, 0.2 mL DHE or DCFH-DA solution (5μM, PBS) was added, and the cells were incubated for 30 min at 37 °C. Afterward, the cells were rinsed again with PBS, and subsequently irradiated with an 808 nm laser (0.6 W/cm^2, 5 min). Cell nuclei were stained with the nuclear dye DAPI. The cells were observed using a high-content analysis system.

In vitro Cytotoxicity of SP94-Fe_3O_4@ICG&DOX Nanoparticles

Hepa1-6 cells were inoculated into 96-well plates at a density of 1×10^4 cells per well, incubated for 24 h, and then incubated with different concentrations of SP94-Fe_3O_4@ICG&DOX nanoparticles for 24, 48, or 72 h. The biocompatibility of the nanoparticles was studied by measuring cell viability using standard CCK-8 and LDH assays.

To evaluate the photocytotoxicity of SP94-Fe_3O_4@ICG&DOX nanoparticles, a CCK-8 assay was performed on Hepa1-6 cells. Hepa1-6 cells were seeded in 96-well plates at a density of 1×10^4 cells per well, cultured at 37 °C in a wet humid atmosphere of 5% CO_2 for 24 h, after which the medium was removed. Fresh medium containing different amounts of SP94-Fe_3O_4@ICG&DOX was added to each well. After incubation for 4 h at 37 °C, cells were washed with PBS and soaked in fresh medium. The experimental group was exposed to 808 nm laser (0.6 W/cm^2, 5 min). During laser exposure, the PDT and PTT effects of SP94-Fe_3O_4@ICG&DOX on Hepa1-6 cells were further verified by maintaining a constant temperature to avoid the PTT effect, or by treating the cells with 100 mM NaN_3 to avoid generating ROS. After irradiation, cells were cultured for an additional 12 h. The dark control group was maintained under the same conditions as the experimental group, except for the irradiation. Cell viability was measured using a CCK-8 assay.

The synergistic PDT/PTT effects of SP94-Fe_3O_4@ICG&DOX nanoparticles on Hepa1-6 cells were further confirmed by co-staining with Calcein AM and propidium iodide (PI). Briefly, Hepa1-6 cells were seeded in 6-well plates at a density of 5×10^4 cells per well. After overnight culture in a humid atmosphere of 5% CO_2 at 37 °C, the cells were soaked in the fresh medium containing SP94-Fe_3O_4@ICG&DOX nanoparticles and further incubated for another 3 h. After washing with PBS (pH7.4), fresh medium was added, and then the cells were exposed to 808 nm laser (0.6 W/cm^2, 5 min). After another 4 h of incubation, live cells were stained with Calcein AM and dead/late apoptotic cells were stained with PI. The stained cells were examined under an inverted microscope (Olympus IX71, Japan).

Animal Model

All animals were cared for in accordance with the "Guidance for the Care and Use of Laboratory Animals". All procedures were approved by the Institutional Animal Care and Use Committee of the Institute of Automation, Chinese Academy of Sciences (permit no. IA21-2203-24). Male BALB/c mice aged 6–7 weeks were purchased from the Vital River Laboratory Animal Technology Corporation (Beijing, China) in 5 cages, which were fed and watered freely in standard cages with a light/dark cycle of 12 h. All animals were acclimated to the new environment for at least 7 days before further experimentation. Hepa1-6 cells (1×10^6) were injected into the hips of the mice to establish subcutaneous tumor models. The ketamine–xylazine mixture was used as an anesthetic to anesthetize the mice throughout the imaging and therapeutic experiments.

Pharmacokinetics Studies

BALB/c mice were injected with SP94-Fe_3O_4@ICG&DOX nanoparticles (100 μL, 0.5 mg/mL) through tail vein. Blood samples (~20 μL) were collected from the orbit of BALB/c mice at different time points (0, 1, 4, 8, 12, 24, and 48 h) after

injection of SP94-Fe_3O_4@ICG&DOX nanoparticles. Each blood sample was dissolved in 980 μL of aqua regia and heated to 100 °C in a water bath. Then it was diluted to a suitable concentration using 0.2% HNO_3. The concentrations of SP94-Fe_3O_4@ICG&DOX nanoparticles in the blood were determined using inductively coupled plasma mass spectrometry (ICP-MS). A blank blood sample without SP94-Fe_3O_4@ICG&DOX nanoparticle injection was used to measure the iron content in the blood and calculate the concentration in the experimental groups. The concentration of SP94-Fe_3O_4@ICG&DOX nanoparticles was expressed as a percentage of injected dose, and the value at the 0 h was defined as 100%.

In vitro and in vivo MPI

For in vitro experiments, the concentration measured was 0.005, 0.011, 0.021, 0.042, 0.084, 0.169, 0.338, 0.675 and 1.35 mM for each group of samples. For in vivo experiments, Hepa1-6 bearing mice were divided into three groups when the tumor volume reached ~ 60 mm^3: (1) Vivotrax (Magnetic Insight, Inc, Alameda, CA) group, n = 3; (2) Fe_3O_4 @ICG&DOX nanoparticle group, n = 3; and (3) SP94-Fe_3O_4@ICG&DOX nanoparticle group, n = 3. Prior to imaging, 50 μL of tracer at a concentration of 0.3 mg/mL was injected into each tumor. MPI images were acquired before and after injection at 4, 8, 24, and 72 h by using an MPI scanner (Magnetic Insight Inc., MOMENTUM^{TM} Imager). Data were analyzed using the VivoQuant software (Invicro, Boston, MA, USA).

Tumor Fluorescence Imaging

The specificity of the SP94 peptide in targeting Hepa1-6 HCC cells was detected using in vivo fluorescence molecular imaging. The SP94-Fe_3O_4@ICG&DOX nanoparticles (100 μL, 0.5 mg/mL) were intravenously injected into the tumor-bearing mice and an in vivo imaging system (IVIS, Caliper Life Sciences, US) was used to precede dynamically for the fluorescence imaging Moreover, Fe_3O_4@ICG&DOX nanoparticles were used as control to test the specific binding of SP94 to the Hepa1-6 tumors and Vivotrax as another control to confirm the excellent MPI capability of our nanoparticles. For ex vivo fluorescence imaging, the organs were placed on a black cardboard and analyzed using the same in vivo imaging system.

In vivo Thermal Imaging and Synergistic Phototherapy

When the tumor size reached approximately 60 mm^3, the mice were randomly divided into six groups (n = 7 in each group) for the different treatments.

Group 1: No laser exposure, intravenous injection of 100 μL PBS.

Group 2: Intravenous injection of 100 μL PBS (pH 7.4, 10 mM), followed by laser exposure of the tumor with a low power density of 0.6 W/cm^2 for 5 min 24 later.

Group 3: No laser exposure, intravenous injection of 100 μL SP94-Fe_3O_4@ICG&DOX.

Group 4: Intravenous injection of 100 μL Fe_3O_4@ICG&DOX, followed by laser exposure with the same parameters as in group 2.

Group 5: Intravenous injection of 50 μL ICG and 50 μL DOX, followed by laser exposure with the same parameters as in Group 2.

Group 6: Intravenous injection of 100 μL SP94-Fe3O4@ICG&DOX, followed by laser exposure with the same parameters as in Group 2. The spot of the laser beam was adjusted according to the shape and size of the tumor. During irradiation, the temperature of the tumor was recorded using an IR camera. After therapy, the tumor sizes and body weights of the mice were measured every three days. The formula for estimating the tumor volume is as follows:

Tumor volume=length x $(width)^2/2$)

The tumor volume was evaluated by normalizing the measured values.

Tumor growth inhibition (TGI) was calculated as follows:

$$TGI\ (\%) = \left(1 - \frac{T_{final} - T_{initial}}{C_{final} - C_{initial}}\right) \times 100$$

Where T is the tumor volume in the agent-treated group, and C represents the tumor volume of the PBS-treated group.

Biocompatibility safety assessment

Blood biochemical analyses and routine blood tests were conducted during the observation period to assess the safety of the main organs (the liver and kidney). After therapy, 5μm sections of the major organs and tumors were stained with hematoxylin and eosin (H&E). The sections were stained with H&E and images were obtained using a biological inverted microscope (Olympus IX71, Japan).

Statistical Analysis

Statistical analyses were performed using Origin8.0. Intergroup differences were analyzed using Tukey's multiple comparison test or the Student's *t*-test. All statistical data are expressed as mean values ± standard deviation (SD), with * indicating P values < 0.05, ** indicating P values <0.01, and *** indicating P values <0.001, all of which were considered statistically significant.

Results and Discussion

Characterization of SP94-Fe_3O_4@ICG&DOX Nanoparticles

The scheme for probe synthesis is shown in Figure 1. Carboxyl-functionalized monodisperse hollow Fe_3O_4 nanoparticles were prepared via high-temperature thermal decomposition and ligand exchange reactions. ICG and DOX were encapsulated in hollow Fe_3O_4 nanoparticles using an extremely simple mixing method at room temperature. The HCC-targeted peptide SP94 was then conjugated to the surface of the monodisperse hollow Fe_3O_4 nanoparticles through a simple coupling reaction. The TEM and SEM images exhibited the well-defined structure of the SP94-Fe_3O_4@ICG&DOX nanoparticles (Figure 2a and b). The shell thickness of the resultant SP94-Fe_3O_4@ICG&DOX nanoparticles was approximately 6 nm and the inner hollow diameter was approximately 7 nm (Figure 2a). The hydrated particle size of the SP94-Fe_3O_4@ICG&DOX nanoparticles was approximately 28.2 nm, which was larger than that of Fe_3O_4@ICG&DOX nanoparticles (22.1 nm) and hollow Fe_3O_4 nanoparticles (24.4 nm) (Figure 2c). This was due to conjugation of the SP94 peptide to the surface of the nanoparticles. The UV-Vis-NIR absorption (Figure 2d) and fluorescence (Figure 2e) spectra of SP94-Fe_3O_4@ICG&DOX nanoparticles were recorded. Two new peaks appeared at 480 nm and 700–900 nm in the UV-Vis-NIR spectrum and at 590 nm (Ex:480 nm) and 816 nm (Ex:785 nm) in the fluorescence spectrum after the encapsulation of ICG and DOX, indicating the successful encapsulation of ICG and DOX into the hollow Fe_3O_4 nanoparticles.

A vibrating sample magnetometer (VSM) was used to measure the magnetic properties of the nanoparticles. As shown in Figure S1, neither coercivity nor remanence was observed in the samples, indicating that the nanoparticles were

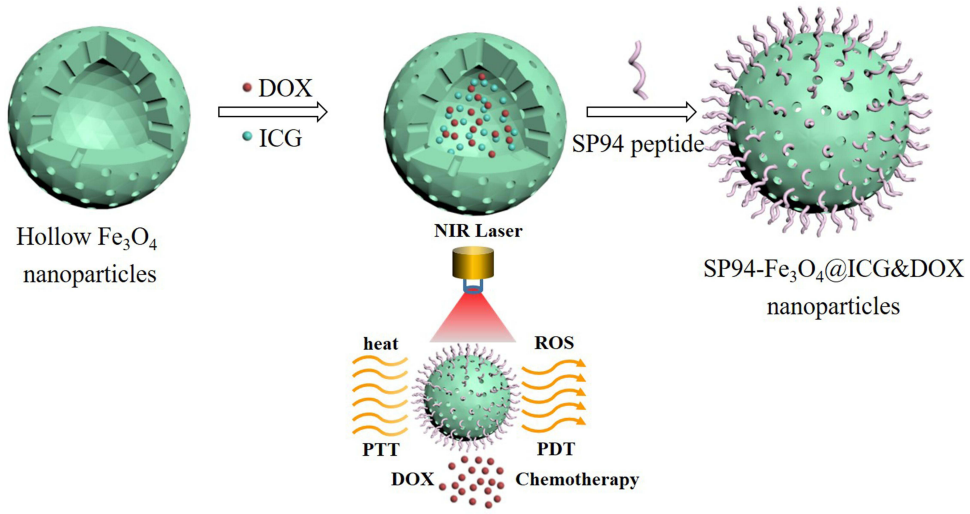

Figure 1 Synthesis of the SP94-Fe_3O_4@ICG&DOX and its application for NIR laser triggered the combination of phototherapy and chemotherapy.

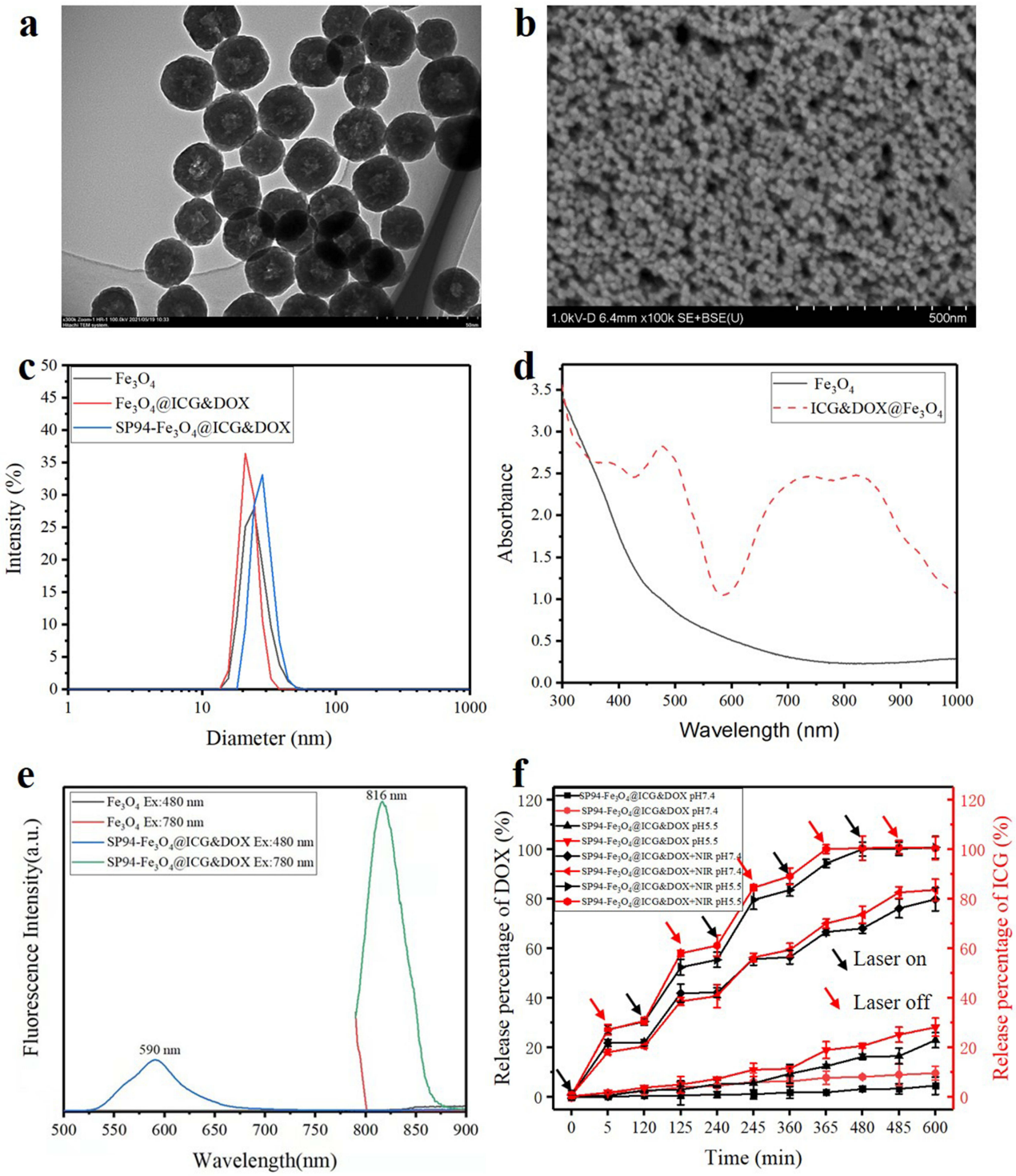

Figure 2 TEM (**a**) and SEM (**b**) of the SP94-Fe_3O_4@ICG&DOX nanoparticles; (**c**) Dynamic light scattering size of the nanoparticles in water (n = 3); Ultraviolet-visible-NIR absorbance spectra (**d**) and fluorescence spectra (**e**) of SP94-Fe_3O_4@ICG&DOX nanoparticles at the indicated concentrations in water; (**f**) DOX and ICG release profile of SP94- Fe_3O_4@ICG&DOX nanoparticles triggered by laser illumination (n = 3).

superparamagnetic. The saturation magnetization (Ms) of SP94-Fe_3O_4@ICG&DOX nanoparticles was 59.88 emu/g and that of hollow Fe_3O_4 nanoparticles was 74.85 emu/g. These data indicated that SP94-Fe_3O_4@ICG&DOX has the potential to be an effective MPI contrast agent. In addition, the pore size distribution of the hollow Fe_3O_4 nanoparticles was in the range 12–26 Å (Figure S2). And the dimensions of the ICG and DOX were 25.0×18.2 Å and 13.4×12.9 Å,

respectively, according to the method reported by Mantina.[41] The opening pores facilitated the diffusion of ICG and DOX into the cavities of hollow Fe_3O_4 nanoparticles. π–π stacking of ICG and DOX occurs in the cavity. The appearance of aggregates was not conducive to outward diffusion from the cavity. The loading efficiencies of the ICG and DOX were 45.2% and 42.7%, respectively. The release profiles of SP94-Fe_3O_4@ICG&DOX under different conditions are shown in Figure 2f. After 10 h, the cumulative drug release rates of DOX and ICG were about 4.6% ± 3.5% and 9.6% ± 2.8% in PBS (pH7.4) and 22.9%±3.0% and 28.2%±3.6% in PBS (pH5.5) without laser irradiation, respectively. However, after irradiation with NIR laser, the fluorescence intensity of ICG in the supernatant increased significantly (Figure S3). And When the nanoparticles were illuminated with NIR laser for 5 min at every time point, the cumulative drug release rates of DOX and ICG were significantly increased (66.6% ± 1.3% and 70.0% ± 1.9% (pH7.4), and 94.3% ± 1.7% and 100.0% ±1.7% (pH5.5) within 6 h, respectively).The enhanced release properties may be due to the heat generated by NIR laser irradiation, and the π–π interaction decreased at a lower pH to promote the disintegration of the ICG and DOX complex and the diffusion of the drug molecules. These results indicated that local NIR laser irradiation and the pH of the surrounding environment may be effective external triggers for inducing controlled targeted drug release.

In vitro Photo-Effects and Photostability of SP94-Fe_3O_4@ICG&DOX Nanoparticles

SP94-Fe_3O_4@ICG&DOX nanoparticles exhibited a broad absorption range of 600–1000 nm (Figure 2d). The initial design of nanoparticles was to achieve targeted photochemotherapy by controlling the release of drugs under laser irradiation and combining photothermal and photodynamic effects (Figure 3a). The photothermal effect of SP94-Fe_3O_4 @ICG&DOX nanoparticles by NIR laser irradiation (808 nm, 0.6 W/cm^2) was investigated (Figure 3b). The temperature elevation of the SP94-Fe_3O_4@ICG&DOX nanoparticles under NIR light irradiation (808 nm, 0.6 W/cm^2) was monitored to evaluate the photothermal conversion. SP94-Fe_3O_4@ICG&DOX nanoparticles exhibited a rapid temperature elevation

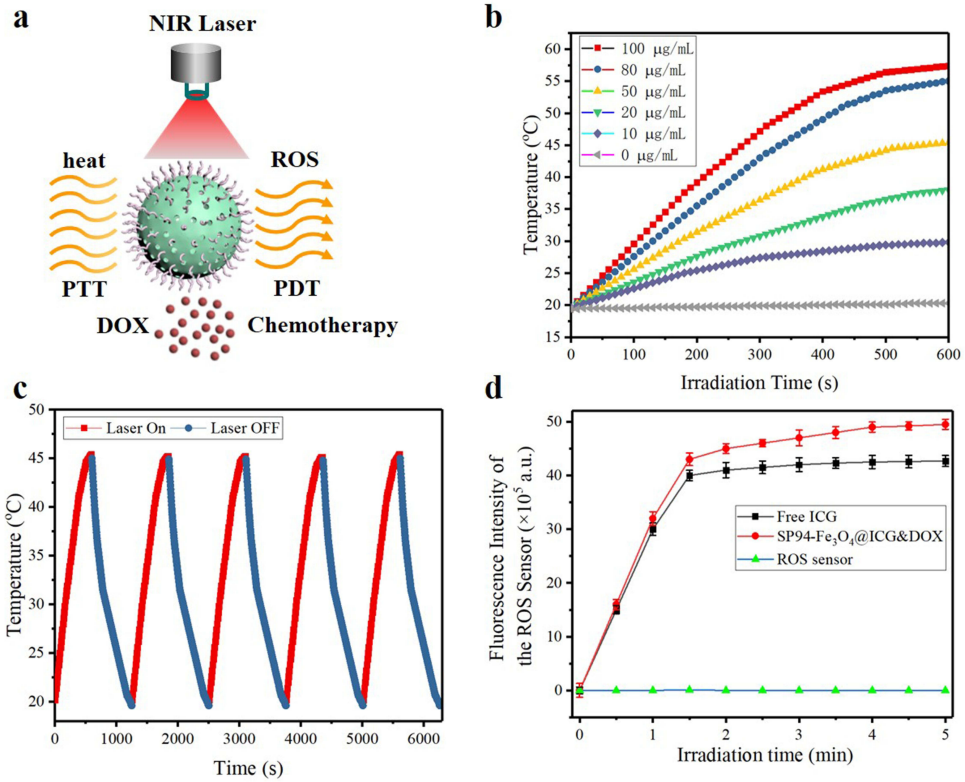

Figure 3 (**a**) Schematic illustration of the SP94-Fe_3O_4@ICG&DOX nanoparticles for therapy; (**b**) Temperature changes of the SP94-Fe_3O_4@ICG&DOX nanoparticles at different concentrations under 808 nm laser irradiation for 10 min and 0.6 W/cm^2; (**c**) The photothermal response of the SP94-Fe_3O_4@ICG&DOX nanoparticles in aqueous solution (both containing 50 μg/mL of the SP94-Fe_3O_4@ICG&DOX nanoparticles) with a NIR laser (808 nm, 10 min, 0.6 W/cm^2), and then the laser was turned off for 11 min. Repeated and recorded five times; (**d**) singlet oxygen generation of SP94-Fe_3O_4@ICG&DOX nanoparticles during single NIR laser irradiation ((808 nm, 0.6 W/cm^2) (n = 5), Concentration of SP94-Fe_3O_4@ICG&DOX nanoparticles is 0.1 mg/mL.

of 10.2 °C at a concentration as low as 10 μg/mL, whereas DI water as a control had no obvious temperature elevation (0.9 °C) (Figure 3b). The photothermal effects of the SP94-Fe_3O_4@ICG&DOX nanoparticles were dependent on irradiation time and nanoparticle concentration. Thus, these factors can be regulated to control the heat generation, which is critical for potent hyperthermia (> 45 °C). The photothermal conversion efficiency of SP94-Fe_3O_4@ICG&DOX nanoparticles was determined using a modified method similar to that reported by Roper.[42] The detailed calculation formulae and data are presented in the Supporting Information (Figure S4). The 808 nm laser photothermal conversion efficiency of SP94-Fe_3O_4@ICG&DOX nanoparticles was 36.9%, which was higher than Au Nanorods (20.7%) and BODIPY derivatives (26.0%) and comparable to most of photothermal semiconductor agents such as CuS nanoparticles. The photostability of SP94-Fe_3O_4@ICG&DOX nanoparticles was characterized after five cycles of heating and cooling. The results showed that SP94-Fe_3O_4@ICG&DOX nanoparticles had excellent photothermal stability, with no significant change observed after five cycles of heating and cooling (Figure 3c). Moreover, no significant difference was observed in the size distribution of the nanoparticles and the TEM images between the fresh prepared SP94-Fe_3O_4@ICG&DOX nanoparticles and the one after laser irradiation for five cycles (Figure S5). These results implied the huge potential of SP94-Fe_3O_4@ICG&DOX nanoparticles for repeated or long-term cancer therapy under NIR laser irradiation.

In addition, we assessed the ROS generation ability of SP94-Fe_3O_4@ICG&DOX nanoparticles during NIR laser exposure using the universal ROS probe DCFH-DA, which can be oxidized by ROS to the highly fluorescent DCF. Under NIR laser irradiation, the fluorescence intensity of the ROS probe without SP94-Fe_3O_4@ICG&DOX nanoparticles or free ICG remained almost unchanged with prolonged irradiation time, whereas a noticeable increase in fluorescence intensity was observed in the presence of SP94-Fe_3O_4@ICG&DOX nanoparticles or free ICG, indicating that our nanoparticles had a favorable ability for ROS generation (Figure 3d).

Cellular Uptake and Photocytotoxicity in vitro

The targeting ability of the SP94-Fe_3O_4@ICG&DOX nanoparticles at the cellular level was assessed using three independent methods. A Prussian blue staining assay was performed to detect cellular uptake efficiency in Hepa1-6 cells. The different probe concentrations had no effect on the cell number, membrane, nucleus, or morphology (Figure 4A). Thus, SP94-Fe_3O_4@ICG&DOX nanoparticles did not exhibit detectable toxicity toward liver cancer cells. After incubation of Hepa1-6 cells with SP94-Fe_3O_4@ICG&DOX nanoparticles, the number of stained cells increased as the concentration of the nanoparticles increased. When the nanoparticle concentration reached 60 μg/mL, the positive rate of Prussian blue staining was approximately 100%. However, as a control, the positive rate of Fe_3O_4@ICG&DOX nanoparticles at a concentration of 60 μg/mL was less than 60%. To track the SP94-Fe_3O_4@ICG&DOX nanoparticles in vivo, confocal microscopy was used to confirm their ability to target HCC cells. After incubation with SP94-Fe_3O_4@ICG&DOX nanoparticles for 4 h, green fluorescence generated by FITC-labelled nanoparticles was clearly observed in tumor cells, and the green fluorescence was enhanced compared to that in the control groups (FITC labelled DOX and FITC labelled Fe_3O_4@ICG&DOX) (Figure 4B). The uptake efficiency of SP94-Fe_3O_4@ICG&DOX nanoparticles in Hepa1-6 cells was further quantified using flow cytometry to measure cell fluorescence after nanoparticle incubation (Figure S6). SP94-Fe_3O_4@ICG&DOX nanoparticles exhibited concentration-dependent cellular uptake, and enhanced fluorescence intensity was achieved with Fe_3O_4@ICG&DOX nanoparticles. Taken together, these data support that SP94-Fe_3O_4@ICG&DOX exerts a good targeting ability in Hepa1-6 cells.

Subsequently, the ability of the SP94-Fe_3O_4@ICG&DOX nanoparticles to generate intracellular ROS and localized hyperthermia, respectively, was observed by staining with DHE, DCFH, and Calcein-AM/PI (Figure 5 and 6). To achieve single PDT and PTT treatments, Hepa1-6 cells were subjected to temperature control to avoid the PTT effect or treated with 100 mM NaN_3 to avoid ROS production during laser irradiation. As shown in Figure 5, in the control group, almost all nuclei displayed blue fluorescence, indicating that laser irradiation alone cannot produce ROS (including superoxide anions (O_2^-) and singlet oxygen ($^1O_2$)) under laser irradiation. However, after incubation with the nanoparticles, some nuclei exhibited orange (Figure 5A) or some cytoplasm exhibited green fluorescence (Figure 5B). Furthermore, the SP94-Fe_3O_4@ICG&DOX nanoparticles resulted in stronger fluorescence under irradiation than Fe_3O_4@ICG&DOX nanoparticles, indicating that the SP94 modified nanoparticles exhibit a higher cellular uptake to generate more intracellular ROS under irradiation, which plays a key role in causing cell damage. As shown in Figure 6A, under an inverted fluorescence

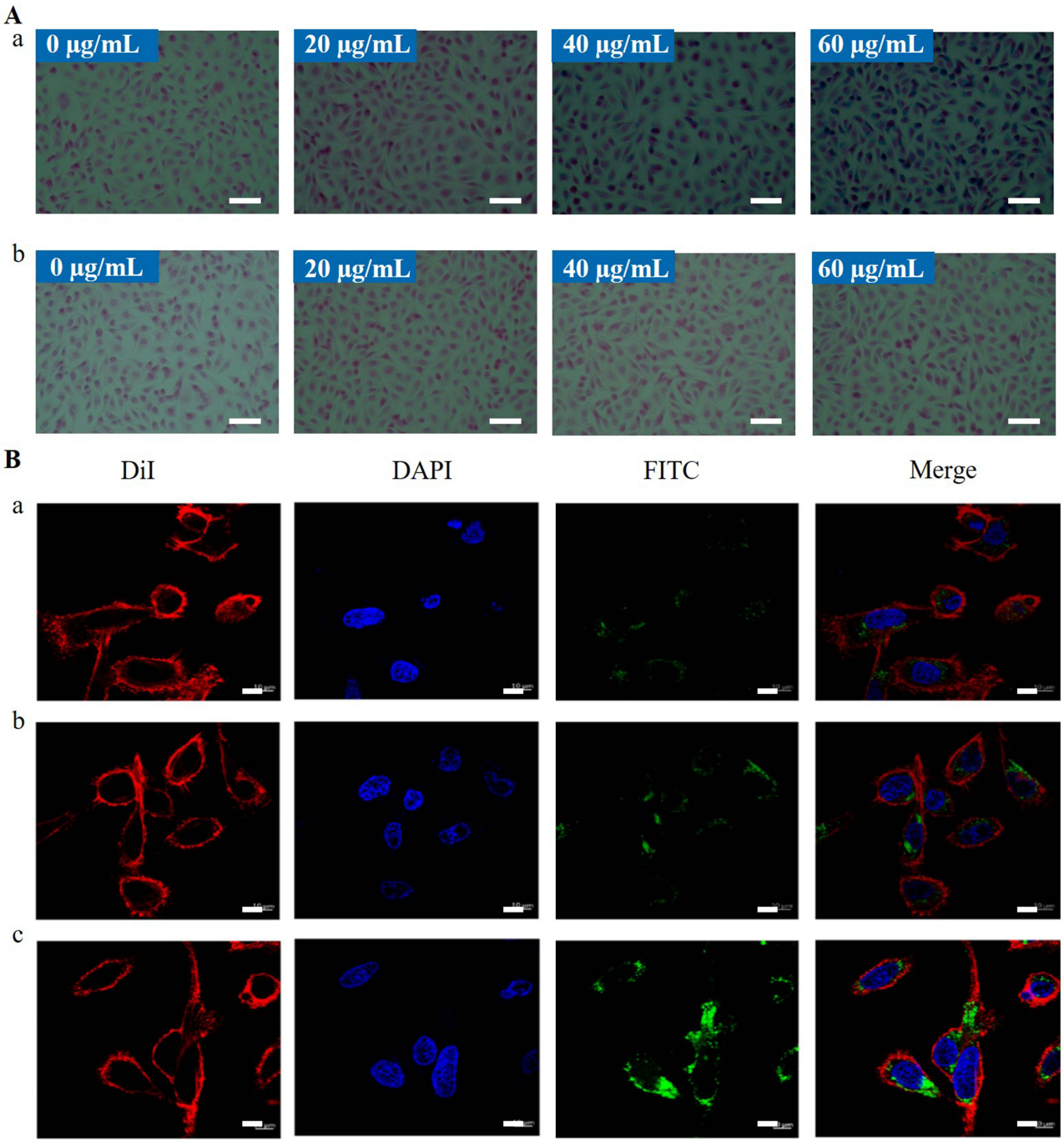

Figure 4 (**A**) Prussian blue-stained images revealed an efficient cellular uptake of SP94-Fe_3O_4@ICG&DOX nanoparticles at incubation concentration of 0, 20, 40 and 60 μg/mL of the nanoparticles for 4 h (blue: nanoparticles, red: cell nucleus) (scale bar = 100 μm): (**a**) SP94-Fe_3O_4@ICG&DOX nanoparticles, (**b**) Fe_3O_4@ICG&DOX nanoparticles; (**B**) Confocal laser scanning microscope images of Hepa1-6 cells after incubating with FITC labelled DOX (scale bar = 10 μm) (**a**), FITC labelled Fe_3O_4 @ICG&DOX nanoparticles (**b**) and FITC labelled SP94-Fe_3O_4@ICG&DOX nanoparticles (**c**) for 4 h at 37 °C.

microscope, red fluorescence regions indicating dead cells were observed only in the presence of both SP94-Fe_3O_4 @ICG&DOX nanoparticles and laser irradiation, indicating that our nanoparticles or laser irradiation alone did not compromise the cell viability. Furthermore, it can be seen that as irradiation time or the concentration of the nanoparticles increased, the red fluorescent region expanded (Figure 6B), indicating the importance of controlling nanoparticles' concentration and laser irradiation time. These results illustrated that some cells in both the PDT and PTT separately

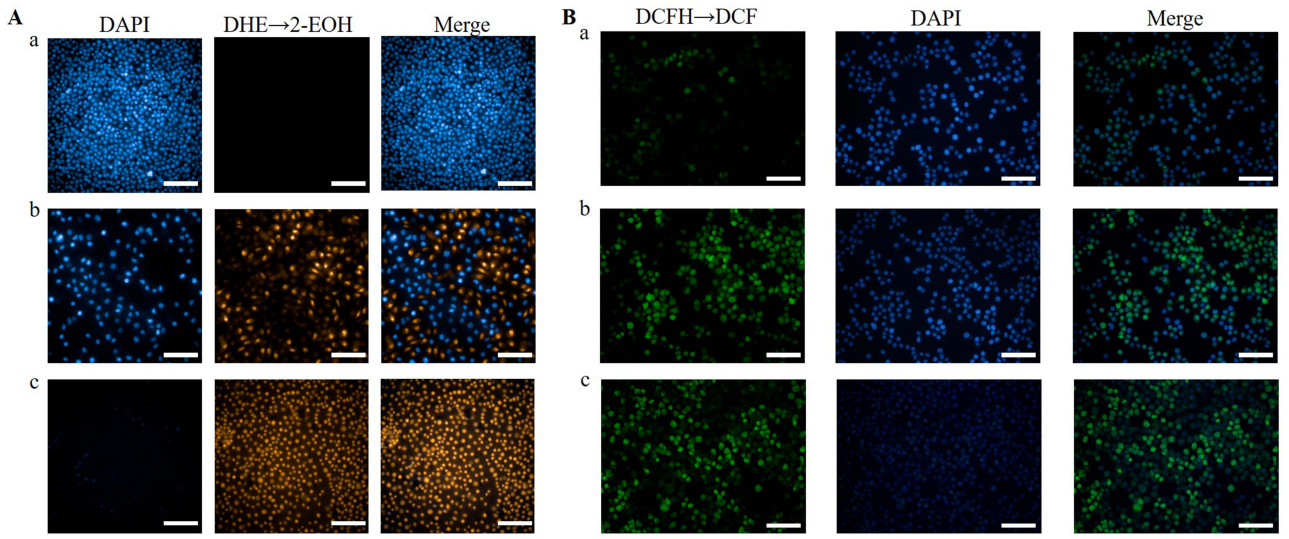

Figure 5 (**A**) Laser-induced superoxide anion (O_2^-) generation and (**B**) laser-induced single oxygen ($^1O_2$) generation of nanoparticles in Hepa1-6 cells: (**a**) PBS, (**b**) Fe_3O_4 @ICG&DOX nanoparticles; (**c**) SP94- Fe_3O_4@ICG&DOX nanoparticles (Scale bar =100 μm).

treated groups were killed and displayed red fluorescence. In addition, our nanoparticles simultaneously provided synergetic PDT/PTT induction, resulting in the death of most cells (Figure 6C).

Furthermore, the biocompatibility of SP94-Fe_3O_4@ICG&DOX was evaluated using the CCK8 and LDH assays (Figure 7a and b). After treatment with our nanoparticles, no significant toxic effect on Hepa1-6 cells was observed in the absence of laser irradiation, and the relative cell viability was between 90 and 100%, even a concentration of 0.1 mg/mL, thus providing sufficient evidence that our nanoparticles could enter into Hepa1-6 cells effectively with good biocompatibility in vitro. However, SP94-Fe_3O_4@ICG&DOX nanoparticles caused severe photo-damage against Hepa1-6 cells (0.82 μg/mL ICG IC_{50}) under laser irradiation, which was much lower than that of Fe_3O_4@ICG&DOX nanoparticles (3.92 μg/mL ICG IC_{50}) (Figure 7c). The IC_{50} of SP94-Fe_3O_4@ICG&DOX nanoparticles without laser irradiation was higher than of 11.00 μg/mL ICG, indicating a significantly reduced cytotoxicity without laser irradiation. And the cytotoxicity of SP94-Fe_3O_4@ICG&DOX nanoparticles was significantly reduced with IC_{50} of 7.00 μg/mL or higher than 11.00 μg/mL ICG with keeping a constant temperature or in the presence of NaN_3 under laser irradiation, suggesting that SP94-Fe_3O_4@ICG&DOX nanoparticles have remarkable synergetic PDT/PTT effect. These results indicate that nanoparticles can effectively cause severe photocytotoxicity. Moreover, the simultaneous synergistic PDT/PTT effect was due to the enhanced cellular uptake of our nanoparticles, efficient ROS generation, and photothermal effect, which were responsible for the enhanced therapeutic efficiency.

Imaging Experiments

To assess MPI performance, we compared SP94-Fe_3O_4@ICG&DOX with commercially available MPI contrast agent (Vivotrax) at different concentrations (Figure 8a). At the same concentration, the two-dimensional (2D) projection MPI image of SP94-Fe_3O_4@ICG&DOX was much higher than that of Vivotrax (Figure 8a). Moreover, the MPI signals of SP94-Fe_3O_4@ICG&DOX showed a linear relationship with nanoparticle concentration (core mass) with a high slope of SP94-Fe_3O_4@ICG&DOX (79.20 mM^{-1}) compared to that of Vivotrax (26.40 mM^{-1}; Figure 8b). To investigate whether SP94-Fe_3O_4@ICG&DOX could perform MPI in vivo, 50 μL of SP94-Fe_3O_4@ICG&DOX nanoparticles, Fe_3O_4 @ICG&DOX nanoparticles, or Vivotrax was injected into the tumors (murine HCC Hepa1-6) of living mice with equal Fe contents, and the signal changes were monitored longitudinally using 2D projection MPI scans. Compared with Vivotrax, the synthesized nanoparticles displayed significantly higher MPI signals after injection (Figure 8c and Figure S7). The MPI signal enhancement of the Fe_3O_4@ICG&DOX nanoparticles was limited to the injection site and gradually decreased over time (Figure 8c). However, the MPI signals of SP94-Fe_3O_4@ICG&DOX nanoparticles were significantly higher than those of Fe_3O_4@ICG &DOX nanoparticles. Most importantly, the MPI signals of the SP94-Fe_3O_4

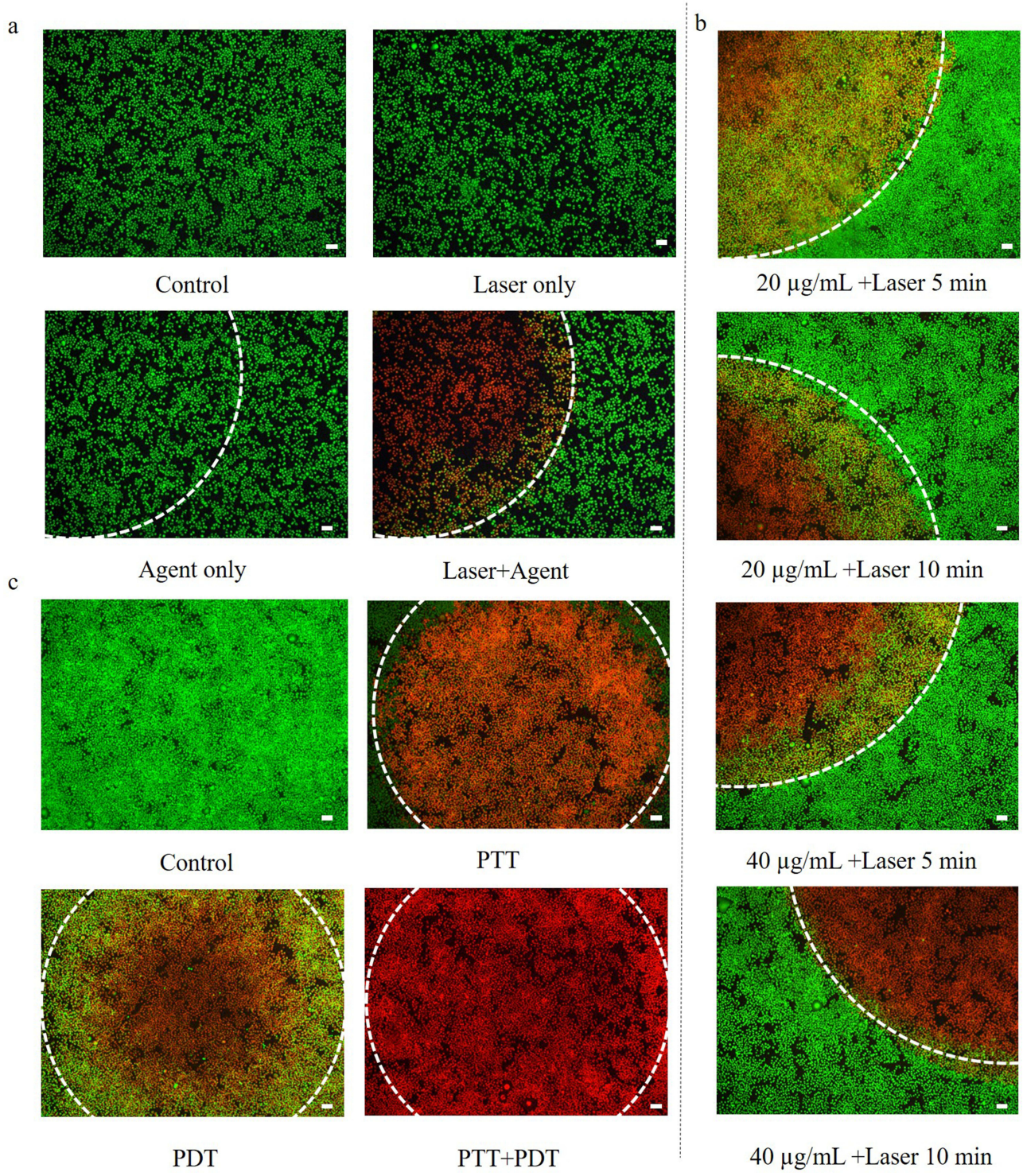

Figure 6 (**a**) In vitro PTT of the SP94-Fe_3O_4@ICG&DOX nanoparticles; (**b**) In vitro photothermal destruction of Hepa1-6 cells treated by various combinations of SP94-Fe_3O_4@ICG&DOX and NIR laser irradiation (808 nm, 0.6 W/cm^2); (**c**) FL images of Hepa1-6 cells after PDT, PTT and simultaneous PDT/PTT treatments. Viable cells were stained green with Calcein-AM, and dead/later apoptosis cells were floating and eluted, or stained red with PI (Scale bar = 50 μm).

@ICG&DOX nanoparticles were more evenly distributed over the tumor site because of the active targeting of the SP94 peptide.

We further tested the SP94-Fe_3O_4@ICG&DOX nanoparticles for targeted fluorescence imaging in vivo using a Hepa1-6 HCC tumor-bearing mouse model. Prior to the nanoparticle injection, BLI images of the same tumor-

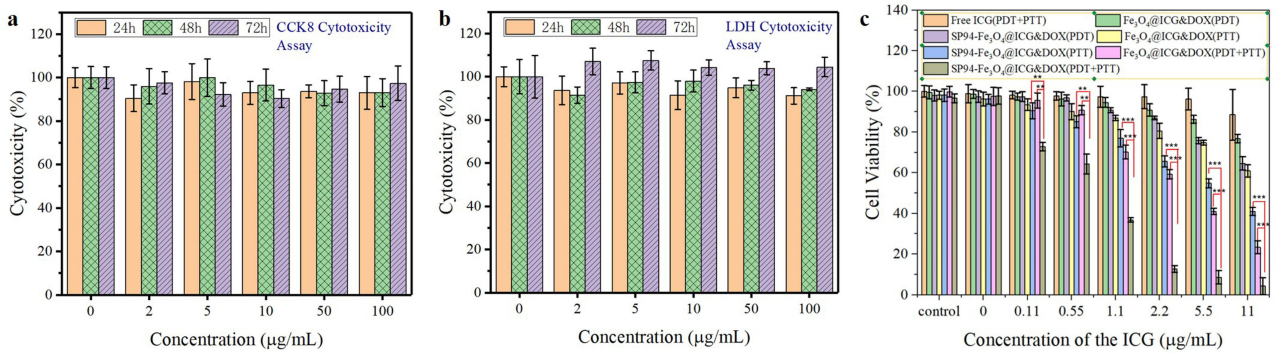

Figure 7 (**a** and **b**) Biocompatibility of the SP94-Fe_3O_4@ICG&DOX nanoparticles detected with different methods (**a**) CCK8 cytotoxicity assay, (**b**) LDH cytotoxicity assay; (**c**) Quantitative detection of Hepa1-6 cells after PDT, PTT and simultaneous PDT/PTT treatments, determined by the standard CCK-8 assay. The data are shown as mean ± SD (n = 3). Significance between every two groups was calculated by the Student's *t*-test. **P*<0.05, ***P*<0.01, and ****P*<0.001.

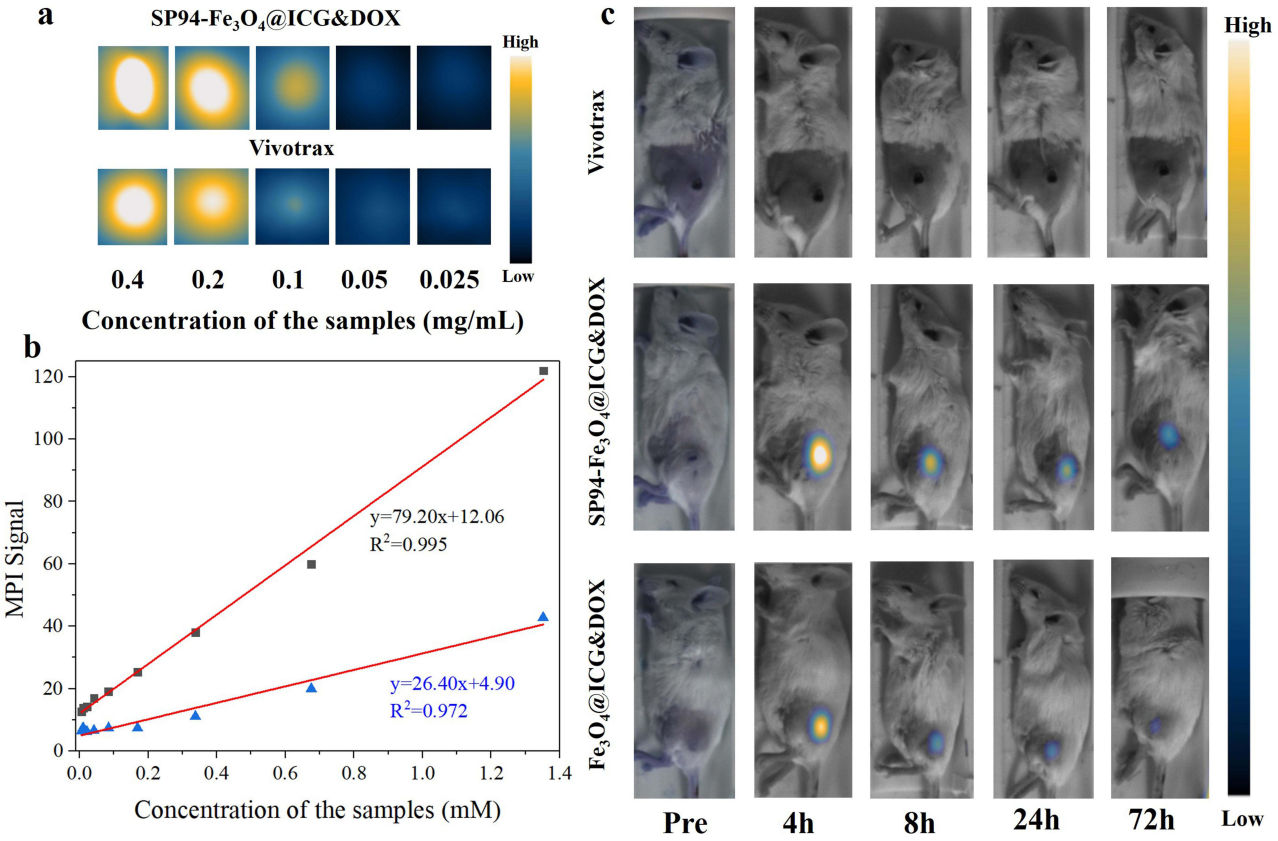

Figure 8 (**a**) In vitro MPI images of the SP94-Fe_3O_4@ICG&DOX and Vivotrax samples with different concentrations; (**b**) Plot of MPI signals of all samples: SP94-Fe_3O_4 @ICG&DOX (■) and Vivotrax (▲); (**c**) In vivo dynamic MPI of mice intratumorally injected with Vivotrax, SP94-Fe_3O_4@ICG&DOX, and Fe_3O_4@ICG&DOX, respectively.

bearing mice were recorded to determine the tumor location. In vivo imaging was performed by intravenous injection of 50 μL SP94-Fe_3O_4@ICG&DOX nanoparticles or Fe_3O_4@ICG&DOX nanoparticles with equal ICG content. Fluorescence signals were collected using an in vivo imaging system (IVIS, Caliper Life Sciences, US). Figure 9a and b show the time course of the NIR fluorescence images of mice after intravenous injection. The fluorescence signals of the tumors were most obvious at 12 h and 48h after SP94-Fe_3O_4@ICG&DOX and Fe_3O_4@ICG&DOX nanoparticle injection, respectively. The ratios of the $S_{tumor}/S_{surrounding\ tissue}$ of SP94-Fe_3O_4@ICG&DOX nanoparticles were higher than those of Fe_3O_4@ICG&DOX nanoparticles, particularly at 12 h (2.48 times) and 24 h (2.30 times) (Figure 9c). Due to the attenuation that occurs during light penetration, ex vivo fluorescence imaging was performed

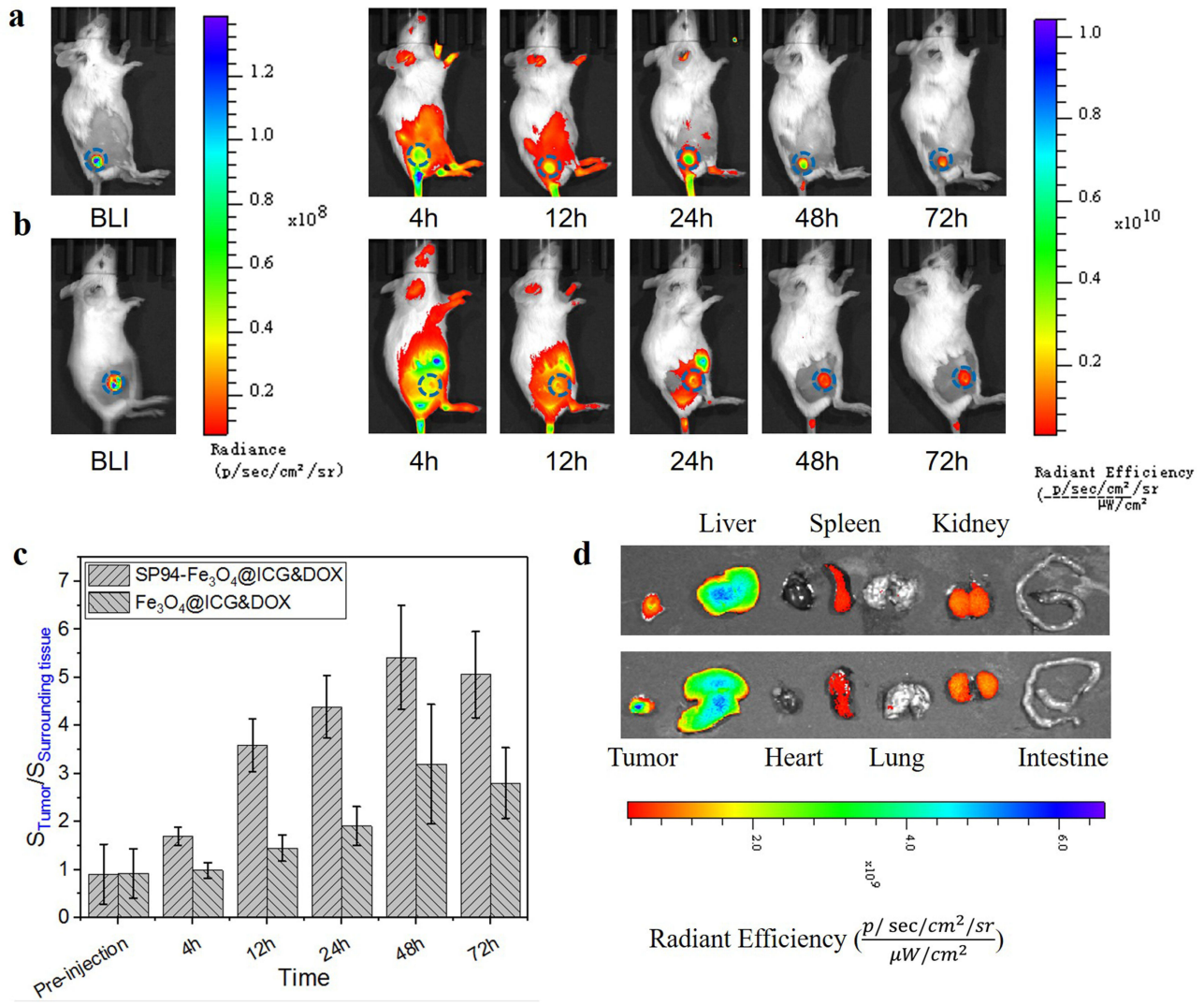

Figure 9 In vivo FL imaging of mice bearing Hepa1-6 tumors after i.v. injection of nanoparticles at different time intervals: (**a**) SP94-Fe_3O_4@ICG&DOX nanoparticles; (**b**) Fe_3O_4@ICG&DOX nanoparticles; (**c**) The ratio of signal of tumor to signal of surrounding tissues of mice bearing Hepa1-6 tumors after i.v. injection of nanoparticles at different time point, data indicate means and standard errors (n = 3), (*) p<0.05, (**)p<0.01; (**d**) Ex vivo FL images of major organs and tumor after injection of Fe_3O_4 @ICG&DOX (top row) and SP94-Fe_3O_4@ICG&DOX (bottom row) nanoparticles at 72 h.

on major organs (including the heart, liver, spleen, lung, kidney, and intestine) and tumors harvested 24 h after injection. As shown in Figure 9d, the nanoparticles accumulated in the liver but not in the tumor (Figure 9d). Furthermore, compared with Fe_3O_4@ICG&DOX nanoparticles, SP94-Fe_3O_4@ICG&DOX nanoparticles accumulated more at the tumor site (2.74-fold) (Figure S8), consistent with in vivo results. However, in the other organs, there was no significant difference between the two groups. In addition, compared to the skin or tumor (ie, 4T1 tumor), Hepa1-6 tumors exhibited more fluorescence signals (Figure S9). Currently, in clinical, non-invasive diagnostic methods for HCC include computed tomography (CT), magnetic resonance imaging (MRI), and contrast-enhanced ultrasound (CEUS). MRI with high diagnostic accuracy and sensitivity is the gold standard for imaging of HCC.[43] The sensitivity and specificity of contrast-enhanced MRI for detecting HCC nodules are 70% and 94%, respectively.[44] However, the sensitivity drops to 60% for lesions <2 cm, and it is even lower for lesions <1 cm.[45] In our experiments, all HCC lesions (<1 cm) were detected by SP94-Fe3O4@ICG&DOX nanoparticles, which indicated our nanoparticles enhanced the detection sensitivity and had great potential in clinical diagnosis of HCC.

In vivo Biocompatibility of SP94-Fe_3O_4@ICG&DOX Nanoparticles

Blood biochemical analysis and routine blood tests were performed to evaluate in vivo biocompatibility of the SP94-Fe_3O_4@ICG&DOX nanoparticles. After systemic administration of SP94-Fe_3O_4@ICG&DOX nanoparticles (100 μL, 0.5 mg/mL, n = 3), biochemical analysis showed that on days 1, 12, and 25, alanine transaminase (ALT), aspartate aminotransferase (AST), and blood urea nitrogen (BUN) levels were within the normal range (Table S1), indicating no significant effect of the nanoparticles on liver and kidney function. Furthermore, the detection of red blood cells (RBC), white blood cells (WBC), platelets (PLT), lymphocytes, hemoglobin (HGB), mean corpuscular hemoglobin concentration (MCHC), mean corpuscular hemoglobin (MCH), and mean corpuscular volume (MCV) at each time point was similar to that of the untreated control group (Table S1). Thus, these results indicate that SP94-Fe_3O_4@ICG&DOX nanoparticles do not induce toxicity in vitro or in vivo and can be considered an effective biocompatible drug for tumor treatment.

In vivo Synergistic Phototherapy and Chemotherapy of HCC

Encouraged by the superior tumor penetration, imaging function, and treatment results in vitro of SP94-Fe_3O_4@ICG&DOX nanoparticles, we expect to apply SP94-Fe_3O_4@ICG&DOX nanoparticles to achieve laser-triggered ultrafast drug release and combination phototherapy and chemotherapy in vivo. The Hepa1-6 tumor model was established to evaluate the synergistic anticancer effects of SP94-Fe_3O_4@ICG&DOX. As shown in Figure 10a and b, after administering SP94-Fe_3O_4@ICG&DOX nanoparticles, the temperature at the tumor site increased rapidly to 65 °C within 5 min of laser irradiation, achieving rapid drug release (Figure 2f) and PTT. However, the temperature change in the tumors was minimal in the PBS group. In addition, as shown in Figure 10c, the tumor volume of the PBS and PBS+ lasers significantly increased, indicating that there was no obvious inhibitory effect on the growth of Hepa1-6 tumors despite laser irradiation. The suppression efficiency of the Fe_3O_4@ICG&DOX nanoparticles + laser group was significantly improved to 79.89%. This could be explained by the accelerated drug release, PDT, and PTT effects caused by NIR irradiation and the tumor environment, resulting in an effective combinational therapy. Additionally, under laser irradiation, mice treated with SP94-Fe_3O_4@ICG&DOX nanoparticles exhibited better antitumor effects, with a suppression rate of up to 100%, which may be attributed to the enhanced tumor-targeting efficiency of the SP94-Fe_3O_4@ICG&DOX nanoparticles. Notably, the survival time of mice in the SP94-Fe_3O_4@ICG&DOX nanoparticles + laser group was longer than that of mice in the other groups (Figure 10d). There have been many similar studies. Professor Yuhao Li fabricated a sorafenib-loaded $Cu_{2-x}Se$ nanoparticles used for photothermal-synergistic targeted therapy of hepatocellular carcinoma.[46] The mice in the experimental group were intravenously (i.v.) injected with 100 μL of the sorafenib-loaded $Cu_{2-x}Se$ nanoparticles for a total of four times on days 21, 24, 27, and 30, and then the tumors were irradiated for 2 min with an 808 nm laser at a density of 1 W/cm^2, two hours after the injection. The tumor suppression rate is lower than 70%. Professor Chihua Fang fabricated epithelial cell adhesion molecule-functionalized Fe_3O_4@Au nanoparticles for coregistered optoacoustic and magnetic resonance imaging and photothermal therapy of hepatocellular carcinoma.[47] The 40-day survival rate of mice after treatment in the experimental group is only 50%. Professor Ke Xu fabricated co-administration of iRGD with sorafenib-loaded iron-based metal-organic framework as a targeted ferroptosis agent for liver cancer therapy.[48] The tumor suppression rate has improved significantly, but it is still below 90%. Compared with these nanoparticles, our nanoparticles exhibited significant advantages in tumor inhibition and survival time.

In addition, Figure 10e demonstrates that the mice in the SP94-Fe_3O_4@ICG&DOX nanoparticles + Laser and Fe_3O_4@ICG&DOX nanoparticles + Laser groups displayed weight gain; however, in the other groups, their body weights showed slight weight loss. These results implied that our nanoparticles can achieve synergistic phototherapy and chemotherapy for HCC and exhibited good prognosis after treatment.

To further elucidate the in vivo photo-damage effect of SP94-Fe_3O_4@ICG&DOX nanoparticles on tumors under irradiation, major organs and tumors were collected 6 h after irradiation, sliced into 5μm sections, and stained with H&E. Figure S10 shows that SP94-Fe_3O_4@ICG&DOX nanoparticles caused severe cell destruction in tumors after irradiation, whereas the free ICG + laser and Fe_3O_4@ICG&DOX+Laser groups exhibited only minor cell destruction. No significant tumor damage was observed in the PBS group with or without irradiation. Moreover, SP94-Fe_3O_4@ICG&DOX

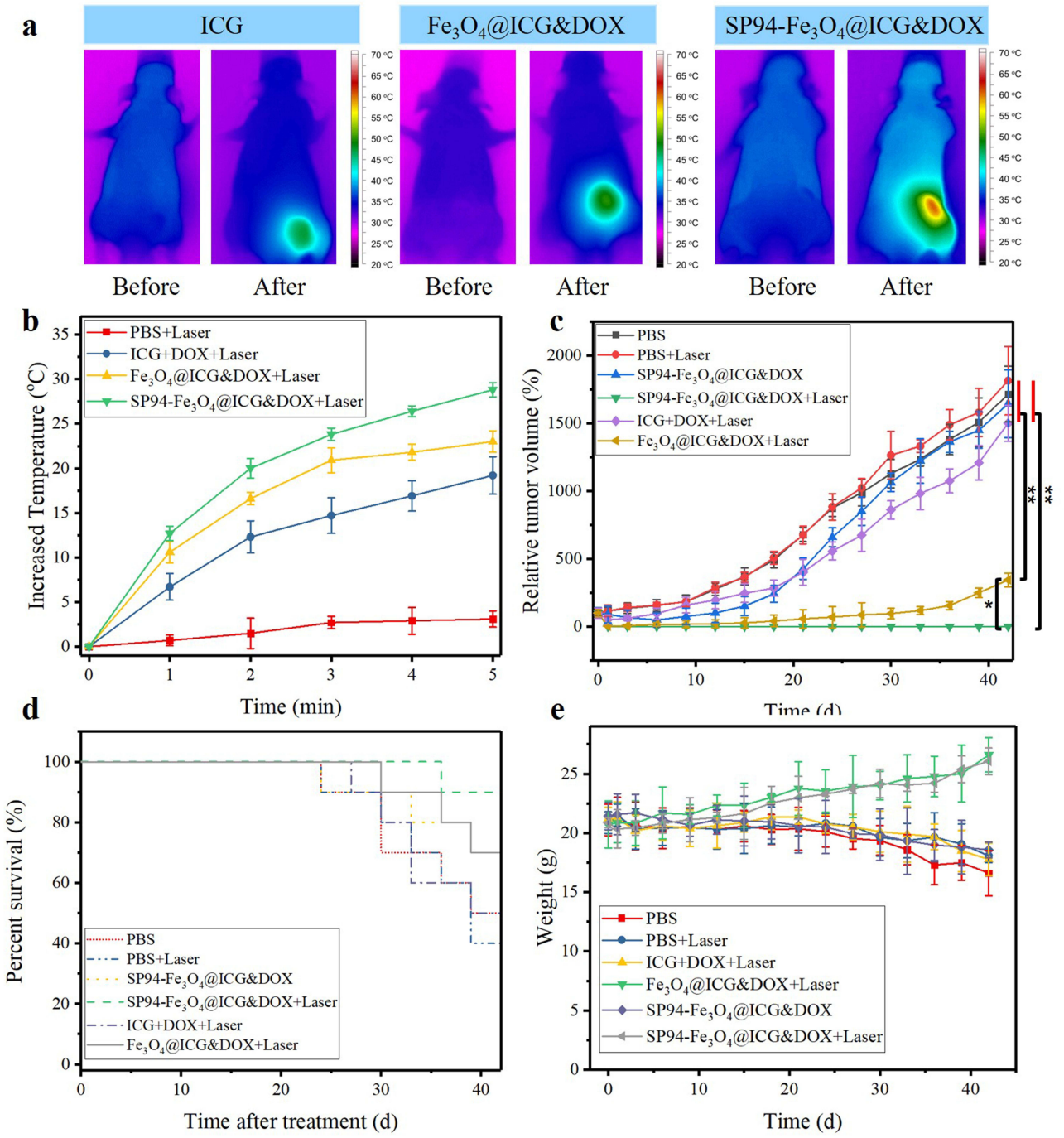

Figure 10 (**a**)Infrared thermography, and (**b**) the increased tumor temperature of tumor-bearing mice treated with SP94-Fe_3O_4@ICG&DOX nanoparticles at 24 h post-injection under 808 nm irradiation at 0.6 W/cm^2 (n = 3); (**c**) Tumor growth inhibition profiles of the mice bearing Hepa1-6 tumor treated with SP94-Fe_3O_4@ICG&DOX, followed by 808 nm irradiation at 0.6 W/cm^2 for 5 min (n = 7); (**d**)Survival rates of mice bearing Hepa1-6 tumors after different treatments; (**e**) Body weights were measured during the 42-day evaluation period in mice under the different conditions (n = 7). Data indicate means and standard errors. (*) p<0.05, (**) p<0.01.

nanoparticles did not cause obvious pathological changes in normal tissues, such as the heart, liver, spleen, lungs, and kidneys (Figure S10). These results again demonstrate the remarkable combination of phototherapy and chemotherapy and the biosafety of SP94-Fe_3O_4@ICG&DOX nanoparticles.

Conclusion

In summary, a multifunctional SP94-Fe_3O_4@ICG&DOX nanoparticle was successfully fabricated, which displayed high biocompatibility and combined targeted and controlled DOX release with excellent photothermal and photodynamic effects to effectively eliminate tumor cells from the primary site. Both in vitro and in vivo experiments demonstrated the excellent tumor imaging capability and enhanced photoinduced cytotoxicity of the SP94-Fe_3O_4@ICG&DOX nanoparticles, which was attributed to the enhanced cellular uptake, sufficient intracellular ROS, and potent photothermal effect under nanoparticle irradiation. The robust and safe nanoparticles exhibited highly efficient accumulation in tumors, excellent in vivo MPI and fluorescence imaging capabilities for precise tumor localization, and synergistic photochemotherapy against tumors under irradiation. We believe that hollow Fe_3O_4 nanoparticle-based nanomedicine systems are promising photochemotherapy diagnostic agents and visual indicators for HCC. And despite the fact that the study was conducted on an animal model, we still hope it could serve as a promising diagnostic agent for use in humans.

The prospective applications of the nanoparticles will be: 1) for early stage HCC without cirrhosis, which was suitable for liver resection, our nanoparticles could effectively diagnose the HCC preoperative using MPI, delineate the margin of the tumor and guide the resection or photo-chemotherapy of the tumor during the tumor through fluorescence imaging to achieve curative treatment; 2) for advanced HCC that is difficult to cure, our nanoparticles could effectively diagnose the HCC using MPI and guide the photo-chemotherapy through fluorescence imaging to delay tumor growth and improve the quality of life of patients.

The main drawback of this method is that the subcutaneous tumor models in immunocompromised mice are useful for studying specific treatment effects, but they lack a comprehensive immune response that includes all immune cell subsets, lymphangiogenesis and chemokine signaling. Thus, in the future work, we will try to choose immunologically humanized mouse models for research to overcome the shortcomings of traditional xenograft models, although the techniques to create these models are challenging.

Data Sharing Statement

The data used and/or analyzed during this study are available from the corresponding author upon reasonable request.

Ethics Approval and Consent to Participate

All animal studies were performed in accordance with the guidelines of the Institutional Animal Care and Use Committee of the Institute of Automation, Chinese Academy of Sciences (permit no. IA21-2203-24). Consent for participation was not applicable.

Acknowledgments

This study was financially supported by the National Natural Science Foundation of China (Grant No.82072098).

Author Contributions

All authors made a significant contribution to the work reported, whether that is in the conception, study design, execution, acquisition of data, analysis and interpretation, or in all these areas; took part in drafting, revising or critically reviewing the article; gave final approval of the version to be published; have agreed on the journal to which the article has been submitted; and agree to be accountable for all aspects of the work.

Disclosure

The authors declare that they have no known competing financial interests or personal relationships that could influence the work reported in this study.

References

1. Balogh J, Victor D, Asham EH., et al. Hepatocellular carcinoma: a review. *J Hepatocellular Carcinoma*. 2016;3:41. doi:10.2147/JHC.S61146
2. Llovet JM, Kelley RK, Villanueva A, et al. Hepatocellular carcinoma. *Nat Rev Dis Primers*. 2021;7(1):6. doi:10.1038/s41572-020-00240-3
3. Yang WS, Zeng XF, Liu ZN, et al. Diet and liver cancer risk: a narrative review of epidemiological evidence. *Br J Nutr*. 2020;124(3):330. doi:10.1017/S0007114520001208

4. Sung H, Ferlay J, Siegel RL, et al. Global Cancer Statistics 2020: GLOBOCAN estimates of incidence and mortality worldwide for 36 cancers in 185 countries. *Cancer J Clin*. 2021;71(3):209. doi:10.3322/caac.21660
5. Wang WY, Wei C. Advances in the early diagnosis of hepatocellular carcinoma. *Genes Dis*. 2020;7(3):308. doi:10.1016/j.gendis.2020.01.014
6. Yun UJ, Bae SJ, Song YR, Kim YW. A critical yap in malignancy of HCC is regulated by evodiamine. *Int J of Mol Sci*. 2022;23(3). doi:10.3390/ijms23031855
7. Cai C, Tian F, Ma JP, Yu ZP, Yang M, Yi CQ. BSA-templated synthesis of Ir/Gd bimetallic oxide nanotheranostics for MR/CT imaging-guided photothermal and photodynamic synergistic therapy. *Nanoscale*. 2023;15(9):4457. doi:10.1039/d2nr06306a
8. Li B, Wang W, Zhao L, et al. Multifunctional AIE nanosphere-based "nanobomb" for trimodal imaging-guided photothermal/photodynamic/pharmacological therapy of drug-resistant bacterial infections. *ACS Nano*. 2023;17(5):4601. doi:10.1021/acsnano.2c10694
9. Ma XX, Huang YR, Chen WJ, et al. J-aggregates formed by NaCl treatment of Aza-coating heptamethine cyanines and their application to monitoring salt stress of plants and promoting photothermal therapy of tumors. *Angew Chem Int Ed Engl*. 2022;62(3):e202216109. doi:10.1002/anie.202216109
10. Tong W, Hui H, Zhang YQ, Tian J, Chen YD. Abstract 10227: high-Sensitive Magnetic Particle Imaging of Intraplaque Hemorrhage for Identification of Unstable Atherosclerotic Plaques. *Circulation*. 2021;144(Suppl_1):A10227. doi:10.1161/circ.144.suppl_1.10227
11. Tong W, Hui H, Shang WT, et al. Highly sensitive magnetic particle imaging of vulnerable atherosclerotic plaque with active myeloperoxidase-targeted nanoparticles. *Theranostics*. 2021;11(2):506. doi:10.7150/thno.49812
12. Yu EY, Bishop MI, Zheng B, et al. Magnetic particle imaging: a novel in vivo imaging platform for cancer detection. *Nano Lett*. 2017;17(3):1648. doi:10.1021/acs.nanolett.6b04865
13. Wang GR, Li WZ, Shi GY, et al. Sensitive and specific detection of breast cancer lymph node metastasis through dual-modality magnetic particle imaging and fluorescence molecular imaging: a preclinical evaluation. *European Journal of Nuclear Medicine and Molecular Imaging*. 2022;49(8):2723. doi:10.1007/s00259-022-05834-5
14. Du Y, Liu XL, Liang Q, Liang X-J, Tian J. Optimization and design of magnetic ferrite nanoparticles with uniform tumor distribution for highly sensitive MRI/MPI performance and improved magnetic hyperthermia therapy. *Nano Lett*. 2019;19(6):3618. doi:10.1021/acs.nanolett.9b00630
15. Lu C, Han LB, Wang JN, Wan JC, Song GS, Rao JH. Engineering of magnetic nanoparticles as magnetic particle imaging tracers. *Chem Soc Rev*. 2021;50(14):8102. doi:10.1039/d0cs00260g
16. Stirrat CG, Alam SR, MacGillivray TJ, et al. Ultrasmall supraparamagnetic particles of iron oxide-enhanced magnetic resonance imaging in the assessment of cellular inflammation after myocardial infarction. *Circulation*. 2014;130:A17328. doi:10.1161/circ.130.suppl_2.17328
17. Wang QY, Ma XB, Liao HW, et al. Artificially engineered cubic iron oxide nanoparticle as a high-performance magnetic particle imaging tracer for stem cell tracking. *ACS Nano*. 2020;14(2):2053. doi:10.1021/acsnano.9b08660
18. Khandhar AP, Ferguson RM, Arami H, Krishnan KM. Monodisperse magnetite nanoparticle tracers for in vivo magnetic particle imaging. *Biomaterials*. 2013;34(15):3837. doi:10.1016/j.biomaterials.2013.01.087
19. Ferguson RM, Minard KR, Khandhar AP, Krishnan KM. Optimizing magnetite nanoparticles for mass sensitivity in magnetic particle imaging. *Med Phys*. 2011;38(3):1619. doi:10.1118/1.3554646
20. Ferguson RM, Minard KR, Krishnan KM. Optimization of nanoparticle core size for magnetic particle imaging. *J Magn Magn Mater*. 2009;321(10):1548. doi:10.1016/j.jmmm.2009.02.083
21. Shen LZ, Li B, Qiao YS. Fe3O4 Nanoparticles in targeted drug/gene delivery systems. *Materials*. 2018;11(2):324. doi:10.3390/Ma11020324
22. Stephen ZR, Dayringer CJ, Lim JJ, et al. Approach to rapid synthesis and functionalization of iron oxide nanoparticles for high gene transfection. *ACS Appl Mater Interfaces*. 2016;8(10):6320. doi:10.1021/acsami.5b10883
23. Jin YS, Ma XB, Zhang S, et al. A tantalum oxide-based core/shell nanoparticle for triple-modality image-guided chemo-thermal synergetic therapy of esophageal carcinoma. *Cancer Lett*. 2017;397:61. doi:10.1016/j.canlet.2017.03.030
24. Jin YS, Wang K, Tian J. Preoperative examination and intraoperative identification of hepatocellular carcinoma using a targeted bimodal imaging probe. *Bioconjug Chem*. 2018;29(4):1475. doi:10.1021/acs.bioconjchem.8b00161
25. van Dam GM, Koller M, Qiu SQ, et al. Phase II in-human dose escalation study of the optical molecular imaging tracer bevacizumab-800cw for molecular fluorescence guided surgery in primary breast cancer patients. *Cancer Res*. 2017;77:4. doi:10.1158/1538-7445.SABCS16-P4-01-01
26. Hain E, Lim C, Malek A, Salloum C, Azoulay D. Indocyanine green-fluorescence imaging in the assessment of intestinal viability during surgery: can fluorescence replace human eye? *Ann Surg*. 2017;265(4):E48. doi:10.1097/SLA.0000000000001170
27. van Dam GM, Themelis G, Crane LMA, et al. Intraoperative tumor-specific fluorescence imaging in ovarian cancer by folate receptor-alpha targeting: first in-human results. *Nature Med*. 2011;17(10):1315. doi:10.1038/nm.2472
28. Zhang YQ, Liu WL, Luo XJ, et al. Novel self-assembled multifunctional nanoprobes for second-near-infrared-fluorescence-image-guided breast cancer surgery and enhanced radiotherapy efficacy. *Adv Sci*. 2023;10(10):e2205294. doi:10.1002/advs.202205294
29. Yang RQ, Wang PY, Lou KL, et al. Biodegradable nanoprobe for nir-ii fluorescence image-guided surgery and enhanced breast cancer radiotherapy efficacy. *Adv Sci*. 2022;9(12). doi:10.1002/Advs.202104728
30. Wang PY, Li JQ, Wei M, et al. Tumor-microenvironment triggered signal-to-noise boosting nanoprobes for NIR-IIb fluorescence imaging guided tumor surgery and NIR-II photothermal therapy. *Biomaterials*. 2022;287:121636. doi:10.1016/j.biomaterials.2022.121636
31. Ge RW, Kao C. Cell surface GRP78 as a death receptor and an anticancer drug target. *Cancers*. 2019;11(11):1787. doi:10.3390/Cancers11111787
32. Lee CH, Tsai HY, Chen CL, et al. Isoliquiritigenin inhibits gastric cancer stemness, modulates tumor microenvironment, and suppresses tumor growth through glucose-regulated protein 78 downregulation. *Biomedicines*. 2022;10(6):1350. doi:10.3390/biomedicines10061350
33. La XQ, Zhang LC, Yang YF, Li HQ, Song GS, Li ZY. Tumor-secreted GRP78 facilitates the migration of macrophages into tumors by promoting cytoskeleton remodeling. *Cell Signal*. 2019;60:1. doi:10.1016/j.cellsig.2019.04.004
34. Li ZW, Li ZY. Glucose regulated protein 78: a critical link between tumor microenvironment and cancer hallmarks. *Biochim Biophys Acta*. 2012;1826(1):13. doi:10.1016/j.bbcan.2012.02.001
35. Dauer P, Sharma NS, Gupta VK, et al. ER stress sensor, glucose regulatory protein 78 (GRP78) regulates redox status in pancreatic cancer thereby maintaining "stemness". *Cell Death Dis*. 2019;10(2):132. doi:10.1038/s41419-019-1408-5
36. Ran DN, Mao JN, Shen Q, et al. GRP78 enabled micelle-based glioma targeted drug delivery. *J Control Release*. 2017;255:120. doi:10.1016/j.jconrel.2017.03.037

37. Zhao YD, Shi DD, Shang MM, et al. GRP78-targeted and doxorubicin-loaded nanodroplets combined with ultrasound: a potential novel theranostics for castration-resistant prostate cancer. *Drug Deliv*. 2022;29(1):203. doi:10.1080/10717544.2021.2023698
38. Jiang B, Zhang RF, Zhang JL, et al. GRP78-targeted ferritin nanocaged ultra-high dose of doxorubicin for hepatocellular carcinoma therapy. *Theranostics*. 2019;9(8):2167. doi:10.7150/thno.30867
39. Farshbaf M, Khosroushahi AY, Mojarad-Jabali S, Zarebkohan A, Valizadeh H, Walker PR. Cell surface GRP78: an emerging imaging marker and therapeutic target for cancer. *J Control Release*. 2020;328:932. doi:10.1016/j.jconrel.2020.10.055
40. Liao YN, Liu Y, Xia XH, et al. Targeting GRP78-dependent AR-V7 protein degradation overcomes castration-resistance in prostate cancer therapy. *Theranostics*. 2020;10(8):3366. doi:10.7150/thno.41849
41. Mantina M, Chamberlin AC, Valero R, Cramer CJ, Truhlar DG. Consistent van der Waals radii for the whole main group. *J Phys Chem A*. 2009;113 (19):5806. doi:10.1021/jp8111556
42. Roper DK, Ahn W, Hoepfner M. Microscale heat transfer transduced by surface plasmon resonant gold nanoparticles. *J Phys Chem C*. 2007;111 (9):3636. doi:10.1021/jp064341w
43. Roberts LR, Sirlin CB, Zaiem F, et al. Imaging for the diagnosis of hepatocellular carcinoma: a systematic review and meta-analysis. *Hepatology*. 2018;67:401. doi:10.1002/hep.29487
44. Zhao C, Dai HY, Shao JW, et al. Accuracy of various forms of contrast-enhanced MRI for diagnosing hepatocellular carcinoma: a systematic review and meta-analysis. *Front Oncol*. 2021;11:680691. doi:10.3389/fonc.2021.680691
45. Semaan S, Violi NV, Lewis S. Hepatocellular carcinoma detection in liver cirrhosis: diagnostic performance of contrast-enhanced CT vs. MRI with extracellular contrast vs. gadoxetic acid. *Eur Radiol*. 2020;30:1020. doi:10.1007/s00330-019-06458-4
46. Huang AT, Du J, Liu ZY, et al. Sorafenib-loaded $Cu_{2-x}Se$ nanoparticles boost photothermal–synergistic targeted therapy against hepatocellular carcinoma. *Nanomaterials*. 2022;12(18):3191. doi:10.3390/nano12183191
47. Wang RX, Zhang SY, Lin YX, et al. Epithelial cell adhesion molecule-functionalized Fe_3O_4@Au nanoparticles for coregistered optoacoustic and magnetic resonance imaging and photothermal therapy of hepatocellular carcinoma. *ACS Appl Nano Mater*. 2022;5(8):10213. doi:10.1021/acsanm.2c01165
48. Liu XC, Zhu XY, Qi X, Meng XW, Xu K. Co-administration of iRGD with sorafenib-loaded iron-based metal-organic framework as a targeted ferroptosis agent for liver cancer therapy. *Int J Nanomed*. 2021;16:1037. doi:10.2147/IJN.S292528